Geophysical Research Letters

RESEARCH LETTER
10.1029/2021GL092762

Importance of Gravity Wave Forcing for Springtime Southern Polar Vortex Breakdown as Revealed by ERA5

Aman Gupta[1], Thomas Birner[1,2], Andreas Dörnbrack[2], and Inna Polichtchouk[3]

[1]Meteorological Institute Munich, Ludwig-Maximilians-Universität München, München, Germany, [2]Deutsches Zentrum für Luft und Raumfahrt (DLR), Institut für Physik der Atmosphäre, Oberpfaffenhofen, Germany, [3]European Centre for Medium-Range Weather Forecasts (ECMWF), Reading, UK

Key Points:

- ERA5 partially resolves gravity waves allowing evaluation of their contribution to the springtime polar vortex breakdown
- Climatology of the gravity wave forcing highlights relevance of gravity wave refraction and oblique propagation and suggests deceleration of up to −8 m/s/day around 60°S
- Deceleration of the vortex due to gravity wave dissipation can be as high as the total necessary deceleration for the vortex breakdown

Supporting Information:

Supporting Information may be found in the online version of this article.

Correspondence to:

A. Gupta,
Aman.Gupta@lmu.de

Citation:

Gupta, A., Birner, T., Dörnbrack, A., & Polichtchouk, I. (2021). Importance of gravity wave forcing for springtime southern polar vortex breakdown as revealed by ERA5. *Geophysical Research Letters*, *48*, e2021GL092762. https://doi.org/10.1029/2021GL092762

Received 29 JAN 2021
Accepted 10 APR 2021

Abstract Planetary waves (PWs) and gravity waves (GWs) are the key drivers of middle atmospheric circulation. Insufficient observations and inaccurate model representation of GWs limit our understanding of their stratospheric contributions, especially during the Antarctic polar vortex breakdown. This study employs the strength of the high-resolution ERA5 reanalysis in resolving a broad spectrum of GWs in southern midlatitudes and its ability to estimate their forcing during the breakdown period. Most of the resolved southern hemisphere GWs deposit momentum around 60°S over the Southern Ocean. Further, a zonal momentum budget analysis during the breakdown period reveals that the resolved GW forcing in ERA5 provides as much as one-fourth of the necessary wind deceleration at 60°S, 10 hPa. The parameterized GW drag, mostly from non-orographic sources, provides more than half of the wind deceleration. Both findings highlight the key role of GWs in the vortex breakdown and discuss possibilities for further stratospheric GW analysis.

Plain Language Summary Strong flow over mountains during winters and instabilities in the southern hemisphere troposphere can excite gravity waves that propagate from near-surface all the way to atmospheric heights of 50–80 km. At these heights, they dissipate momentum and decelerate the strong eastward winds. Knowing the structure and extent of the forcing by these waves can help to better understand their role in driving the stratospheric and mesospheric circulation. However, the net forcing by these waves is not accurately known on account of limited observations and because global climate models cannot sufficiently resolve them. This study illustrates that the high-resolution ERA5 reanalysis, which forms a natural bridge between observations and free running climate models, can be used to estimate the mean forcing due to such gravity waves and can help assess their role in springtime deceleration of polar vortex. Such an analysis was not possible using previous reanalysis datasets due to low resolution. The findings show that, indeed, gravity wave forcing can provide a large fraction of the deceleration needed to slow down the strong westerly winds in late winters.

1. Introduction

Planetary waves (PW) and gravity waves (GW) are the key drivers of middle atmospheric circulation and variability by transporting momentum from the surface to stratospheric and mesospheric altitudes. In the stratosphere, PWs predominantly drive the wintertime circulation by mixing potential vorticity in the winter middle and high latitudes (Haynes et al., 1991; Holton et al., 1995). In the mesosphere, however, GWs are the main driver of the pole-to-pole global circulation (Becker, 2012; Holton, 1982; Plumb, 2002).

GWs are ubiquitous in the stratosphere (Fritts & Alexander, 2003) and have been shown to play an important role in the southern springtime polar vortex breakdown (de la Cámara et al., 2016; McLandress et al., 2012). Here, the breakdown is defined as the westerly-to-easterly transition of zonal winds at 60°S and 10 hPa in the Austral spring. PWs and GWs, in concert with radiative adjustment, govern the dynamical evolution of the stratospheric circulation during the breakdown period (de la Cámara et al., 2016). Additionally, PWs and GWs are coupled and interact with each other (Holton, 1984).

Comprehensive climate models do not adequately resolve the GW spectrum relevant for the stratospheric circulation. Most of the GW forcing in models is approximately represented by Orographic (O-) and Non-Orographic (NO-) Gravity Wave Drag (GWD) parameterizations (Lott & Miller, 1997; Orr et al., 2010; Scinocca, 2002, 2003). The approximate representation of GWs, however, prevents a sound analysis of

planetary wave–gravity wave interactions in the stratosphere. The representation of GWs is sensitive to the choice of parameterization scheme, model resolution, model tuning procedure, etc. (Garcia et al., 2017; Hourdin et al., 2017).

The necessity for accurate model representation of GWs is further emphasized by the "cold-pole" bias problem among comprehensive climate models. The vortex breakdown could be delayed by up to 3–4 weeks compared to the observed breakdown date (Garcia et al., 2017; Lu et al., 2020). Studies investigating this model bias point to an inaccurate representation of GWs in these models. More precisely, "missing" GW forcing from small unresolved islands in the Southern Ocean (Alexander & Grimsdell, 2013; Garfinkel & Oman, 2018; McLandress et al., 2012), under-resolved NO-GW sources around 60°S (Shibuya et al., 2015) or from underrepresented OGWD is considered to provide a substantial deceleration of the vortex (de la Cámara et al., 2016; Plougonven et al., 2020).

In this study, we use the zonal momentum budget to assess the contribution of GWs to the Antarctic vortex breakdown using ERA5. ERA5 is the latest reanalysis product from the European Center for Medium-Range Weather Forecasts (ECMWF) (Hersbach et al., 2020) available over a period of 1979-present.

ERA5 assimilates and uses decades of earth system observations to constrain model forecast and variability, and does so using a high-resolution forecast model. Thus, ERA5 provides a bridge between (sparse and spectrally limited) GW observations from satellites and field campaigns (Alexander et al., 2008; Ern et al., 2018; Fritts et al., 2016; Grubišić et al., 2008; Hertzog et al., 2008; Rapp et al., 2020; Wu & Eckermann, 2008) and unconstrained high-resolution models (e.g., Sato et al., 2012; Polichtchouk et al., 2018), which can potentially resolve mesoscale GWs.

The zonal mean zonal wind equation, in Transformed Eulerian Mean (TEM) form, is expressed as (Andrews et al., 1987):

$$\overline{u}_t = \underbrace{\left(f - \frac{1}{R\cos\phi}(\overline{u}\cos\phi)_\phi\right)\overline{v}^*}_{\text{Cor}} \underbrace{- \overline{u}_p\overline{\omega}^*}_{\text{vAdv}} + \underbrace{\frac{1}{R\cos\phi}\vec{\nabla}\cdot\vec{F}}_{\text{EPFD}} + \underbrace{\overline{X}}_{\text{PGWD}} \tag{1}$$

where ϕ is the latitude, p is pressure, t is time, the overbar denotes zonal mean along constant pressure surfaces, and the subscripts denote partial derivative with respect to the variable. f is the Coriolis parameter, $\overline{u}$ is the zonal mean zonal wind, $\overline{v}^*$ and $\overline{\omega}^*$ are the residual meridional and vertical velocities, respectively, $\overline{X}$ is the parameterized gravity wave drag, R is the radius of the earth, and $\vec{F}$ is the Eliassen-Palm (EP)-flux vector given by:

$$\vec{F} = \left(F^{(\phi)}, F^{(p)}\right) = R\cos\phi\left(-\overline{u'v'} + \overline{u}_p\frac{\overline{v'\theta'}}{\overline{\theta}_p}, \left(f - \frac{1}{R\cos\phi}(\overline{u}\cos\phi)_\phi\right)\frac{\overline{v'\theta'}}{\overline{\theta}_p} - \overline{u'\omega'}\right) \tag{2}$$

where θ is the potential temperature and v and ω are the meridional and vertical (pressure) velocities, respectively.

The TEM form of the momentum equation separates the forcing of the mean flow into contributions due to advection by the mean residual circulation and wave forcing. Note that generally horizontal and vertical advection are small compared to the Coriolis torque contained in the Cor term. The EP-flux divergence term (EPFD) and the parameterized drag term (PGWD) collectively represent the net forcing of the mean flow exclusively due to momentum deposition by the resolved (planetary + gravity) waves and the unresolved (orographic + non-orographic gravity) waves, respectively.

The term $-\overline{u'\omega'}_p$ within the total EPFD includes the net forcing of the mean flow by the resolved wave fluxes due to gravity waves (Fritts & Alexander, 2003). We use this term to estimate the wave forcing due to resolved GWs by considering the covariance only from zonal wavenumbers $k_x = 21$ and higher as:

$$VMFC \triangleq -\overline{u'\omega'}_p(k_x \geq 21) = -\left(\Sigma_{k_x \geq 21}\mathrm{Re}\left[\hat{u}(k_x,\phi,p,t)\hat{\omega}^*(k_x,\phi,p,t)\right]\right)_p, \tag{3}$$

where the ()* denotes the complex conjugate of the Fourier coefficient. Hereafter, we refer to the quantity in Equation 3 as the vertical momentum flux convergence (VMFC).

Perturbations associated with $k_x \sim 20$ are associated with length scales of $L = 1{,}000$ km around 60°S, and thus, the contributions from wavenumbers 21 and higher are associated with the wide range of GWs manifested at the largest inertial scales (~1,000 km) all the way to the grid scale, where hyperdiffusion is acting (Shutts & Vosper, 2011).

We use 6-hourly ERA5 temperature, velocity, and zonal wind tendency to assess the momentum budget and VMFC from 2000 to 2019 on model levels at a horizontal resolution of 0.3 × 0.3 (~30 km). For the native output grid, this corresponds to a minimum resolved wavelength of ~ 60–70 km. However, due to scale-selective hyperdiffusion, the effective minimum wavelength will be quite larger than 60–70 km. ERA5 employs a total of 137 unevenly spaced full model levels and has 60 levels between 0.01 and 100 hPa with level spacing varying from ~0.25 km in the lower stratosphere to ~1.5 km near 1 hPa (Hersbach et al., 2020; Hennermann & Guillory, 2020). At this resolution, ERA5 holds potential to resolve a broad spectrum of stratospheric GWs and associated fluxes (as in Equation 3) (Watanabe et al., 2015).

To illustrate ERA5's capability to resolve GWs and to provide a point of direct comparison to observational studies (Ern, et al., 2004 and Kaifler et al., 2020), we show GWs as temperature perturbations at 1.5 hPa (45 km) from ERA5 around 17 July 2012 in Figure 1a. The perturbation profile, obtained by removing the contribution from the first 20 zonal wavenumbers from the full ERA5 temperature field, shows OGWs over both the Andes and the Antarctic Peninsula.

The figure shows propagation and convergence of the OGWs away from their sources and around 60°S, as pointed out by previous studies (Preusse et al., 2002; Sato et al., 2012). OGWs excited over the Andes and the Antarctic peninsula provide a substantial forcing to the mean flow during Austral winters. A strong deceleration of the polar night jet from 140 ms^{-1} down to 80 ms^{-1} eastward of the wave packets is noticed in Figure 1a, highlighting the prominent effect the mesoscale OGWs have on the mean flow.

The distribution of phase lines along the red straight line with markers in Figure 1a shows shearing and refraction of the wave packets into the jet core as they propagate upward and leeward (Figures 1b and 1c). Signs of constructive and destructive interference of waves from both the sources are spotted near 1 hPa in Figure 1b as the phase lines from both regions converge around 60°S. Subsequently, the waves predominantly propagate zonally rather than meridionally before dissipating (Figure 1a).

Figure 1 markedly highlights ERA5's capability in resolving a significant spectrum of mesoscale GWs, a striking contrast to both JRA55 and MERRA2, which have respective horizontal resolutions of 55 and 50 km (Fujiwara et al., 2017), and ERA-Interim, the previous reanalysis product from ECMWF (Dee et al., 2011). This unique capability forms the basis of our inquiry and allows us to estimate the contribution of GWs to the stratospheric vortex breakdown.

2. Gravity Wave Forcing During the Vortex Breakdown

In this section, we assess the strength and structure of the deceleration due to resolved and parameterized GWs in the southern polar stratosphere in ERA5.

We show the flux of potential energy ($\rho_0\overline{\Phi'v'}$, $-g^{-1}\overline{\Phi'\omega'}$) (using black arrows) due to resolved GWs for the 17 July 2012 event at 12 UTC and 18 UTC in Figures 1d and 1e, respectively. Here, Φ' is the geopotential perturbation associated with zonal wavenumbers 21 and above, ρ_0 is the background density and g is the acceleration due to gravity. The tilted arrows indicate oblique, poleward propagation of potential energy over a broad range of latitudes from 40°S to 60°S associated with the Andes. In addition, equatorward energy flux associated with the GWs over Antarctic peninsula between 70°S and 60°S in (d) and 75°S and 60°S in (e) is noticed. The obliquely propagating flux is most likely associated with the orographic waves. Even for individual wave events over Andes or the Antarctic peninsula, not shown here, refraction of GWs and momentum flux into regions of strong zonal flow around 60°S is noticed.

The VMFC [colors in Figures (1d and 1e)] shows the spatial structure and magnitude of the forcing associated with the GW fluxes. Substantial deceleration of up to 15 m/s/day is noticed from 50°S to 70°S near 1 hPa

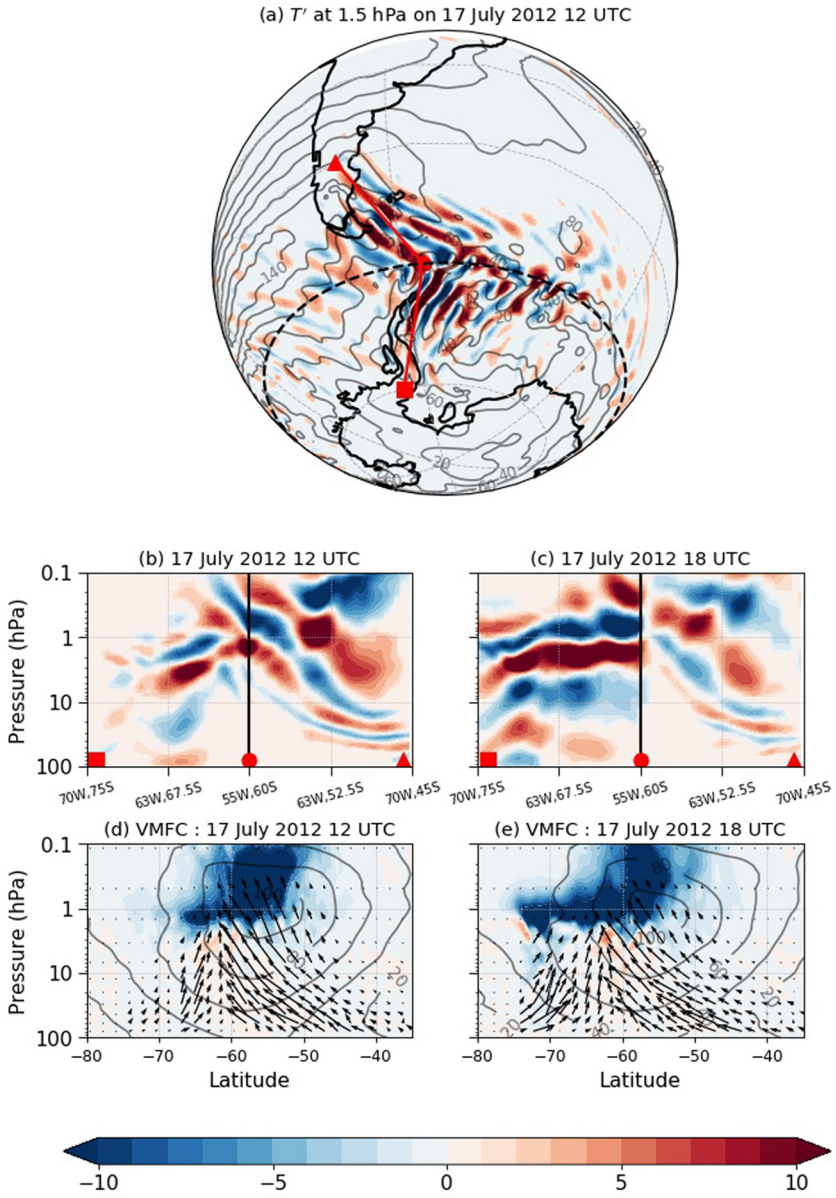

Figure 1. (a) Temperature perturbations (in K) and zonal winds (in ms^{-1}) at 1.5 hPa on 17 July 2012 in ERA5. (b and c) Temperature perturbation cross-section along the solid red line in subplot (a) showing the evolution of temperature perturbation at 12 UTC and 18 UTC on 17 July 2012. The red markers correspond to the respective locations along the red line in subplot (a). (d and e) Potential energy flux vectors (in arrows) for 12 UTC and 18 UTC on 17 July 2012 superimposed over VMFC (in color) with units of ms^{-1} day^{-1}. The black contours indicate zonal wind speeds. The subplots share the same colorbar but have different units. Contributions from zonal wavenumber 20 and below were filtered to calculate GW perturbations and geopotential perturbations Φ'.

and 50°S to 65°S above 0.6 hPa. Throughout most winters, deceleration at 60°S, like shown here for 17 July 2012, is mostly provided by GWs (both orographic and non-orographic) converging around this latitude and by the action of the strong sponge layer starting at 1 hPa that results in the resolved GWs depositing their momentum there.

Hereon, we focus on the gravity wave forcing during the vortex breakdown period in particular. We compute a composite of the resolved drag (VMFC) associated with zonal wavenumbers 21 and higher, over a 50-day lag to a 10-day lead period around the breakdown dates (i.e., westerly-to-easterly transition at 60°S and 10 hPa). We show the 2000–2019 composite averaged resolved GWD (in color) and the parameterized

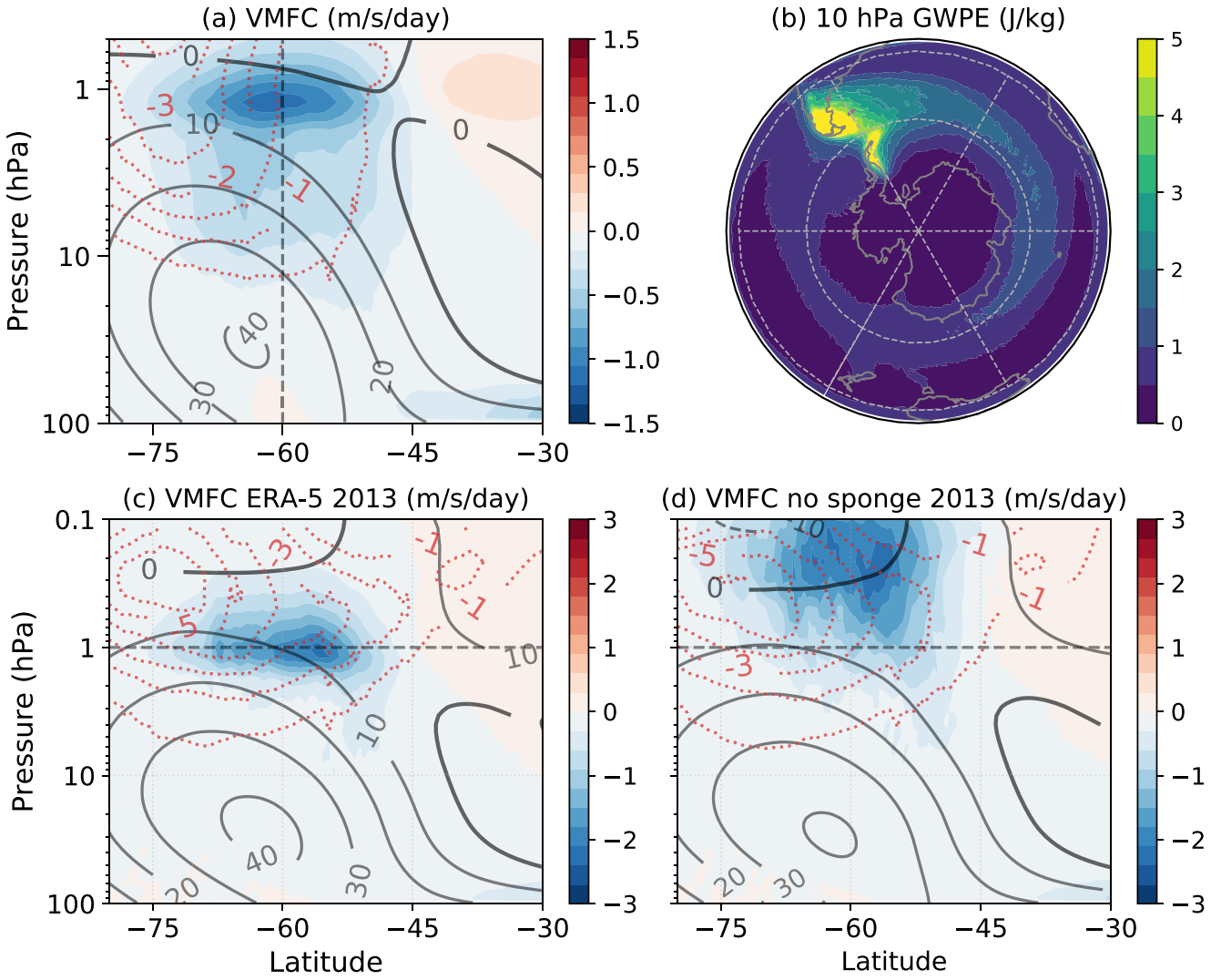

Figure 2. Composite evolution of (a) vertical momentum flux convergence (VMFC) $-\overline{u'\omega'}_p$ for zonal wavenumbers 21 and higher (in ms^{-1} day^{-1}) around the vortex breakdown date (in color). (b) The 2000–2019 averaged gravity wave specific potential energy (GWPE) (in J kg^{-1}) at 10 hPa for September–October–November months. Subplots (c) and (d) show the average VMFC during the breakdown period for the year of 2013 (c) with and (d) without the mesospheric sponge above 1 hPa. The dotted red lines in (a), (c), and (d) show the parameterized drag from the forecast model (in ms^{-1} day^{-1}). The black curves in (a), (c), and (d) show the zonal mean zonal wind speeds (in ms^{-1}).

O + NO GWD drag (in dotted red) in Figure 2a. The resolved GWD in ERA5 extends from 10 hPa all the way up to 0.1 hPa and from 45°S to 75°S, with a maximum at around 60°S and 1 hPa where it provides a forcing of up to −1.5 ms^{-1} day^{-1}. A VMFC intercomparison across five reanalyses: ERA5, JRA55, MERRA2, ERA-Interim, and ERA20 C (Figure S1) shows a much stronger resolved GWD in ERA5, further confirming a significantly broader GW spectrum resolved in ERA5. This improvement in resolved GWD in ERA5 is possible due to significantly improved horizontal and vertical resolution in ERA5.

The parameterized drag provides a stronger deceleration but has a similar latitudinal extent showing a maximum at around 75°S, noticeably poleward of the resolved drag maximum. It should be noted that almost all of the parameterized drag between 55°S and 65°S is from NOGWD, due to little to no contribution from orographic drag over the Southern Ocean (as in Polichtchouk et al. (2018), which used identical model configuration and GWD tuning used to produce ERA5).

The horizontal distribution of GW activity is visualized by the gravity wave *specific* potential energy (GWPE; units J/kg) in Figure 2b. GWPE $= \left(g^2 / 2N^2\right)\left(\overline{\theta'^2} / \overline{\theta}^2\right)$], where g is the acceleration due to gravity, N is the

Brunt–Väisälä frequency. GWPE can be directly computed from satellite and LIDAR observations of temperature, for example, de la Torre et al. (2006) and Hendricks et al. (2014), and provides a direct comparison to gravity waves in models.

Key sources of gravity waves can be seen in GWPE as two separate hotspots over the southern tip of Andes and the Antarctic Peninsula, in Figure 2b. Minor contributions from over New Zealand and Tasmanian islands are also noticed. GWPE is propagated away from these hotspots by the strong westerlies and forms – together with non-orographic sources such as storm tracks and flow instabilities – a GWPE belt around 60°S, which spans much of the latitude circle (Hendricks et al., 2014). As the winter recedes, the GWPE decreases, and the zonal extent of the belt reduces for the months of October and November (not shown). The convergence of GW energy at 60°S, however, is still noticeable well up to the vortex breakdown, explaining the strong VMFC around 60°S in Figure 2a.

The VMFC climatology in Figure 2a shows a maximum around 1 hPa. The accumulation of drag around 1 hPa is not a coincidence as this is the level where the mesospheric sponge in ERA5 comes into effect and extends all the way to the model top (0.01 hPa). The sponge is employed to reduce artificial wave reflection from the rigid lid and is associated with very strong, scale-dependent damping which increases with height and wavenumber. For instance, for wavenumbers 21 and higher, the damping timescale could be as fast as 1 h, rapidly damping most of the GWs entering the mesosphere. Thus, the numerical damping might produce a slightly different VMFC climatology from that observed in the mesosphere.

A similar maximum around 1 hPa is seen in Figure 2c, which shows the VMFC profile from ERA5 for a single year 2013. The role of sponge is highlighted by Figure 2d, which shows the VMFC for 2013 when the ECMWF forecast model was integrated without the mesospheric sponge. While the sponge in ERA5 tends to damp the GWs as soon as they enter the mesosphere (Figure 2c), without the sponge the dissipation occurs at higher altitudes (0.1–0.5 hPa). Thus, the upper boundary treatment in ERA5 still presents a challenge to studying life cycle of GWs in the mesosphere. Nevertheless, we note that the mesospheric sponge does not significantly impact our stratospheric momentum budget analysis in this study below 1 hPa.

Figures 1 and 2 demonstrate that the GWs, despite being generated elsewhere, can contribute to the wind evolution and wave forcing around 60°S. The strong vortex winds here provide more favorable propagation conditions for the GWs, which have a tendency to be refracted into the jet center as they propagate in the vertical (Dunkerton, 1984; Sato et al., 2012). This results in the waves being frequently directed toward the 60°S band, which despite having no surface orographic features, witnesses a convergence of gravity wave momentum during Austral winters.

3. Composite Evolution of Momentum Budget Around Vortex Breakdown

In this section, we assess the composite evolution of different zonal momentum forcing contributions (terms in Equation 1) around 60°S, from 50 days prior to 10 days after the breakdown. Here, the vortex breakdown event, represented by $\tau = 0$ in the following figures, is identified as the day of westerly-to-easterly transition of zonal winds at 60°S and 10 hPa.

We first focus on the planetary scale evolution, that is, the Coriolis acceleration of the mean meridional circulation (Cor in Equation 1) and the deceleration by PWs. The deceleration by PWs can be estimated by removing the resolved GW forcing, VMFC, from the total resolved wave forcing, that is, as the difference EPFD − VMFC. If the vortex breakdown is primarily driven by planetary scale wave dissipation, partially compensated by Coriolis acceleration, we would expect Cor + (EPFD − VMFC) to account for most of the zonal mean flow change. The composite evolution of this sum is shown in Figure 3a.

The composite shows downward migration of a predominantly eastward forcing (acceleration) due to the large-scale contributions from near 1–10 hPa. From 50 to 30 days before the breakdown, a positive momentum forcing is provided by the sum, Cor + EPFD − VMFC, in the upper stratosphere. The positive component of the sum is almost exclusively provided by the Coriolis torque, which represents the steady-state response of the planetary system to *all* of the resolved + parameterized wave forcing. That is, any increase in the resolved or parameterized wave forcing will be compensated by an increase in the Coriolis torque on

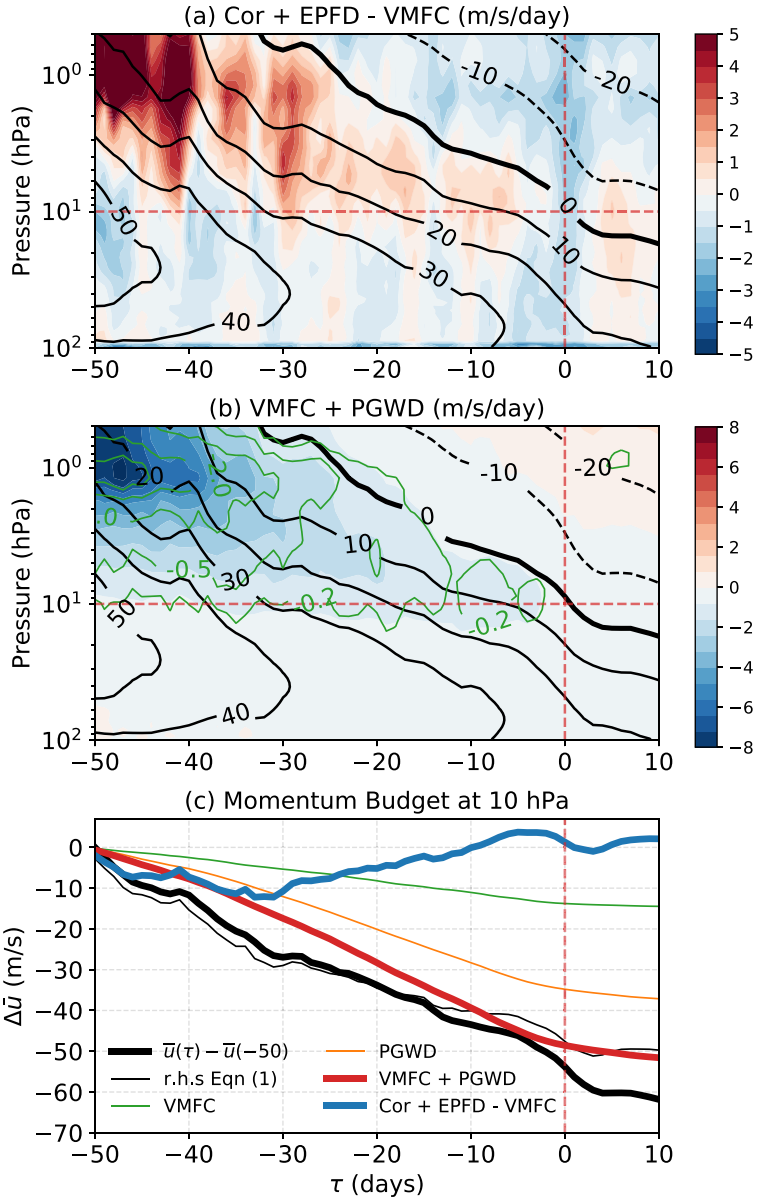

Figure 3. Composites around the vortex breakdown period (in color) for (a) Coriolis acceleration + planetary wave dissipation (term Cor + EPFD − VMFC in Equation 1) and (b) the resolved + parameterized drag (VMFC + PGWD in Equation 1) with units of ms^{-1} day^{-1}. The fields were averaged from 55°S to 65°S and from 2000 to 2019. The black contours in (a) and (b) show the 55°S to 65°S averaged zonal mean zonal wind speed. The green contours in (b) show the resolved gravity wave drag (VMFC) with units ms^{-1} day^{-1}. The subplot (c) shows the time integrated net vortex deceleration (bold black), VMFC (green), parameterized drag PGWD (orange), Cor + EPFD − VMFC (bold blue) and VMFC + PGWD (bold red). The thin solid black curve shows the net sum of all the terms on the right hand side of Equation 1. The thin black curve also considers the zonal mean forcing from 6-hourly velocity increments $\Delta u_{inc}/\Delta t = (u_{analysis} - u_{forecast})/\Delta t$, where $\Delta t = 6$ Hr. All quantities were integrated from lag time $\tau = -50$ days to a lag time τ and have units of ms^{-1}. The dashed vertical red line in all subplots marks the vortex breakdown date.

the system, and vice versa. The upper limit of the positive forcing follows the zero wind line throughout. Approaching the breakdown date, the net forcing weakens but is still positive. A weak but vertically uniform deceleration by the large scales is noticed only at the breakdown date. Even though the large-scale balance, Cor + EPFD − VMFC, provides a gentle positive forcing of the mean flow throughout, it should be noted that the individual steady deceleration provided by the PWs is significantly stronger in magnitude (up to -10 ms^{-1} day^{-1} and forms the primary source of deceleration of the vortex; Figure S2).

Similar to PW forcing, the forcing due to GWs also provides a persistent deceleration during the breakdown period, as shown by the composite map of total resolved + unresolved GW drag, VMFC + PGWD (Figure 3b). A maximum in the GWD is obtained near 1 hPa, 50 days prior to the breakdown. As the vortex weakens, the drag migrates downwards as well, tracing the zero wind line (bold black). The total gravity wave contribution from the sum, (VMFC + PGWD), provides a significant wind deceleration. In fact, the contribution from GWs toward the vortex deceleration can be as high as 40% of the contribution from PWs around 60°S (Figures S2i and S2j).

The role of GWs is shown more clearly in Figure 3c, which compares the *cumulative* momentum change from both the planetary-scales, and the resolved and unresolved small-scales (GWD). A near closure of the budget is obtained, as is indicated by the solid and dashed black curves which respectively show the net deceleration of the mean flow (l.h.s of Equation 1) and the sum of individual terms in the momentum equation (r.h.s of Equation 1). The term Cor + EPFD − VMFC shows substantially weak contribution toward the net deceleration as most of the deceleration by PWs is balanced by a similar Coriolis acceleration. The large-scale balance, however, clearly reveals the key contribution of GWs to the breakdown.

While PWs forcing provide the strongest deceleration of the vortex (up to −10 m/s/day), almost all of the remaining deceleration is provided by GWs (red curve in Figure 3c). Collectively, VMFC (green) and PGWD (orange), provide more than three-fourths of the required net mean flow deceleration (bold red and bold black respectively in Figure 3c). This highlights the important role played by GWs, alongside PWs, in the vortex breakdown.

The large-scales (blue) and the small-scales (red) provide comparable deceleration up to 30 days before the breakdown. Subsequently, the large-scales provide a net acceleration to the mean flow instead while the small-scales continue to decelerate it. During this period, a monotonic deceleration by both the resolved (green) and parameterized (orange) forcing is noticed all the way to the breakdown date.

The latitude-pressure structure of the large-scale and small-scale evolution during two separate periods is shown in Figure S3. During both the intervals, the Cor + EPFD − VMFC term provides acceleration (Figures S3a and S3c) and the resolved + parameterized GWD provides deceleration (Figures S3b and S3d) in the upper stratosphere. 30–50 days before the breakdown, the mean large-scale acceleration of the zonal winds is limited to the upper stratosphere ($p \leq 5$ hPa) and a net deceleration is noticed at 60°S and 10 hPa. 10–30 days before the breakdown, however, the acceleration is restricted to lower altitudes and henceforth a net acceleration is noticed at 60°S and 10 hPa as well. Moreover, for both intervals, a similar structure for both the GWD (in color) and the net vortex deceleration (black curves) is noticed (Figure S3b and S3d), illustrating the role of GWD throughout the upper stratosphere.

4. Conclusion and Discussion

Our analysis establishes the applicability of the current high-resolution reanalysis for climatological gravity waves analyses in the southern polar stratosphere. We used this capability to gain insights into the role of GWs during the Antarctic polar vortex breakdown.

We illustrated leeward propagation and refraction of mountain waves away from Andes and Antarctic peninsula using temperature perturbations in ERA5. These mountain waves deposit momentum and energy away from their sources and along the 60°S zonal band (Preusse et al., 2002; Sato et al., 2012). The resolved GWs in ERA5 allowed an investigation into the mean springtime forcing provided by the GWs. The climatological analysis of VMFC and GWPE for the breakdown period forms a natural extension to the analysis of Sato et al. (2012), which used a high resolution model but only over a 3-year period. The analysis can also be valuable for tuning OGWD and NOGWD parameterizations in climate models.

A further analysis around 60°S based on the momentum budget and composite analysis demonstrated the relative importance of GWs during the breakdown by providing quantitative estimates of their contributions. GWs provide a steady deceleration throughout the breakdown period. This is unlike the combined Coriolis + planetary wave forcing terms, which provide a net deceleration at 60°S and 10 hPa 30–50 days prior to the breakdown, but henceforth provide a net acceleration of the mean flow instead. The balance between the large-scale terms reveals that the GWs cause most of the *necessary* deceleration of the mean

flow around 60°S (red curve in Figure 3). In fact, while the resolved GWs provide around one-fourth of the net deceleration around 60°S and 10 hPa, the parameterized drag provides more than half of the deceleration there (Figure 3c). The orographic parameterization in ERA5 does not consider leeward propagation of the parameterized GWs. Therefore, we note that the parameterized drag around 60°S is almost exclusively due to non-orographic sources like midlatitude storm-tracks and local instabilities (Hendricks et al., 2014; Jewtoukoff et al., 2015; Shibuya et al., 2015).

Dissipation by planetary waves provides the strongest vortex deceleration and is largely balanced by the Coriolis acceleration throughout the winter stratosphere. However, the resolved + unresolved GW forcing in the upper stratosphere is still as strong as 40% of the planetary wave forcing in magnitude around 60°S (Figure S2).

The relative contribution of orographic versus non-orographic sources toward the total GW forcing is unclear and requires further investigation. Our analysis, however, highlights the need for an improved representation of GWs in global circulation models to ensure an accurate wave representation in the stratosphere. This can be achieved either by integrating the models at a high-resolution or by a more accurate model representation of GWs through better parameterizations. For instance, leeward propagation (Figure 1), ignored by OGW parameterizations, could contribute to the "cold-pole" bias in climate models by underestimation of the parameterized GWD around 60°S.

Even though we obtain an approximate closure in the momentum budget analysis at 60°S and 10 hPa in ERA5, an intercomparison across five different reanalyses, not shown, suggests that most reanalyses fail to obtain a closure in the momentum budget in the upper stratosphere ($p \leq 5$ hPa), poleward of 50°S–60°S. The difficulty in closure could be due to differences in the employed OGWD and NOGWD parameterizations, which do not consider realistic generation and propagation of GWs through a vertically and horizontally sheared mean flow (discussed in Plougonven et al. [2020]).

ERA5 resolving a broad spectrum of mesoscale GWs opens avenues for further explorations in stratospheric wave-mean flow interactions. For instance, it allows investigating the net driving of the stratospheric circulation by GWs through the downward control calculations (Haynes et al., 1991; Polichtchouk et al., 2018). It can also allow investigating compensation between planetary wave and gravity wave driving of the stratospheric circulation (Cohen et al., 2013) and studying the coupling between the planetary and gravity waves across scales (Holton, 1984; Polichtchouk et al., 2018) using a potential vorticity framework.

Data Availability Statement

ECMWF's ERA5 data can be freely accessed from https://www.ecmwf.int/en/forecasts/datasets/reanalysis-datasets/era5

Acknowledgments
This research was partly funded by the Deutsche Forschungsgemeinschaft (DFG) via the project MS-GWaves (GW-TP/DO 1020/9-1, PACOG/RA 1400/6-1) and by the German research initiative "Role of the middle atmosphere in climate" (ROMIC) under Grant 01LG1206A provided by the Federal Ministry for Education and Research. Access to ECMWF data was granted through the special project "Deep Vertical Propagation of Internal Gravity Waves."

References

Alexander, M. J., Gille, J., Cavanaugh, C., Coffey, M., Craig, C., Eden, T., et al. (2008). Global estimates of gravity wave momentum flux from high resolution dynamics limb ounder observations. *Journal of Geophysical Research*, *113*(D15). https://doi.org/10.1029/2007JD008807

Alexander, M. J., & Grimsdell, A. W. (2013). Seasonal cycle of orographic gravity wave occurrence above small islands in the Southern Hemisphere: Implications for effects on the general circulation. *Journal of Geophysical Research - D: Atmospheres*, *118*(20), 11589–11599. https://doi.org/10.1002/2013JD020526

Andrews, D., Leovy, C., & Holton, J. (1987). Middle atmosphere dynamics (1st ed., Vol. 40)

Becker, E. (2012). Dynamical Control of the Middle Atmosphere. *Space Science Reviews*, *168*(1), 283–314. https://doi.org/10.1007/s11214-011-9841-5

Cámara, A. d. l., Lott, F., Jewtoukoff, V., Plougonven, R., & Hertzog, A. (2016). On the gravity wave forcing during the southern stratospheric final warming in LMDZ. *Journal of the Atmospheric Sciences*, *73*(8), 3213–3226. https://doi.org/10.1175/JAS-D-15-0377.1

Cohen, N. Y., Gerber, E. P., & Buhler, O. (2013). Compensation between resolved and unresolved wave driving in the stratosphere: Implications for downward control. *Journal of the Atmospheric Sciences*, *70*(12), 3780–3798. https://doi.org/10.1175/JAS-D-12-0346.1

Dee, D. P., Uppala, S. M., Simmons, A. J., Berrisford, P., Poli, P., Kobayashi, S., et al. (2011). The ERA-Interim reanalysis: Configuration and performance of the data assimilation system. *Quarterly Journal of the Royal Meteorological Society*, *137*(656), 553–597. https://doi.org/10.1002/qj.828

de la Torre, A., Schmidt, T., & Wickert, J. (2006). A global analysis of wave potential energy in the lower stratosphere derived from 5 years of GPS radio occultation data with CHAMP. *Geophysical Research Letters*, *33*(24). https://doi.org/10.1029/2006GL027696

Dunkerton, T. J. (1984). Inertia-gravity waves in the stratosphere. *Journal of the Atmospheric Sciences*, *41*(23), 3396–3404. https://doi.org/10.1175/1520-0469(1984)041⟨3396:IWITS⟩2.0.CO;2

Ern, M., Preusse, P., Alexander, M. J., & Warner, C. D. (2004). Absolute values of gravity wave momentum flux derived from satellite data. *Journal of Geophysical Research*, *109*(D20). https://doi.org/10.1029/2004JD004752

Ern, M., Trinh, Q. T., Preusse, P., Gille, J. C., Mlynczak, M. G., Russell, III, J. M., & Riese, M. (2018). GRACILE: A comprehensive climatology of atmospheric gravity wave parameters based on satellite limb soundings. *Earth System Science Data*, *10*(2), 857–892.

Fritts, D. C., & Alexander, M. J. (2003). Gravity wave dynamics and effects in the middle atmosphere. *Reviews of Geophysics*, *41*(1). https://doi.org/10.1029/2001RG000106

Fritts, D. C., Smith, R. B., Taylor, M. J., Doyle, J. D., Eckermann, S. D., Dörnbrack, A., et al. (2016). The Deep Propagating Gravity Wave Experiment (DEEPWAVE): An airborne and ground-based exploration of gravity wave propagation and effects from their sources throughout the lower and middle atmosphere. *Bulletin of the American Meteorological Society*, *97*(3), 425–453. https://doi.org/10.1175/BAMS-D-14-00269.1

Fujiwara, M., Wright, J. S., Manney, G. L., Gray, L. J., Anstey, J., Birner, T., et al. (2017). Introduction to the SPARC reanalysis intercomparison project (S-RIP) and overview of the reanalysis systems. *Atmospheric Chemistry and Physics*, *17*(2), 1417–1452. https://doi.org/10.5194/acp-17-1417-2017

Garcia, R. R., Smith, A. K., Kinnison, D. E., Cámara, Á. D. L., & Murphy, D. J. (2017). Modification of the gravity wave parameterization in the whole atmosphere community climate model: Motivation and results. *Journal of the Atmospheric Sciences*, *74*(1), 275–291. https://doi.org/10.1175/JAS-D-16-0104.1

Garfinkel, C. I., & Oman, L. D. (2018). Effect of gravity waves from small islands in the Southern Ocean on the Southern Hemisphere Atmospheric Circulation. *Journal of Geophysical Research - D: Atmospheres*, *123*(3), 1552–1561. https://doi.org/10.1002/2017JD027576

Grubišić, V., Doyle, J. D., Kuettner, J., Mobbs, S., Smith, R. B., Whiteman, C. D., et al. (2008). The terrain-induced rotor experiment: A field campaign overview including observational highlights. *Bulletin of the American Meteorological Society*, *89*(10), 1513–1534. https://doi.org/10.1175/2008BAMS2487.1

Haynes, P. H., McIntyre, M. E., Shepherd, T. G., Marks, C. J., & Shine, K. P. (1991). On the "downward control" of extratropical diabatic circulations by eddy-induced mean zonal forces. *Journal of the Atmospheric Sciences*, *48*(4), 651–678. https://doi.org/10.1175/1520-0469(1991)048⟨0651:OTCOED⟩2.0.CO;2

Hendricks, E. A., Doyle, J. D., Eckermann, S. D., Jiang, Q., & Reinecke, P. A. (2014). What is the source of the stratospheric gravity wave belt in austral winter? *Journal of the Atmospheric Sciences*, *71*(5), 1583–1592. https://doi.org/10.1175/JAS-D-13-0332.1

Hennermann, K., & Guillory, A. (2020). *What are the changes from ERA-interim to ERA5? - copernicus knowledge base - ECMWF confluence wiki*. Retrieved from https://confluence.ecmwf.int/pages/viewpage.action?pageId=74764925

Hersbach, H., Bell, B., Berrisford, P., Hirahara, S., Horányi, A., Muñoz-Sabater, J., et al. (2020). The ERA5 global reanalysis. *Quarterly Journal of the Royal Meteorological Society*, *146*(730), 1999–2049. https://doi.org/10.1002/qj.3803

Hertzog, A., Boccara, G., Vincent, R. A., Vial, F., & Cocquerez, P. (2008). Estimation of gravity wave momentum flux and phase speeds from quasi-Lagrangian stratospheric balloon flights. Part II: Results from the Vorcore campaign in Antarctica. *Journal of the Atmospheric Sciences*, *65*(10), 3056–3070. https://doi.org/10.1175/2008JAS2710.1

Holton, J. R. (1982). The role of gravity wave induced drag and diffusion in the momentum budget of the mesosphere. *Journal of the Atmospheric Sciences*, *39*(4), 791–799. https://doi.org/10.1175/1520-0469(1982)039⟨0791:TROGWI⟩2.0.CO;2

Holton, J. R. (1984). The generation of mesospheric planetary waves by zonally asymmetric gravity wave breaking. *Journal of the Atmospheric Sciences*, *41*(23), 3427–3430. https://doi.org/10.1175/1520-0469(1984)041⟨3427:TGOMPW⟩2.0.CO;2

Holton, J. R., Haynes, P. H., McIntyre, M. E., Douglass, A. R., Rood, R. B., & Pfister, L. (1995). Stratosphere-troposphere exchange. *Reviews of Geophysics*, *33*(4), 403–439. https://doi.org/10.1029/95RG02097

Hourdin, F., Mauritsen, T., Gettelman, A., Golaz, J.-C., Balaji, V., Duan, Q., et al. (2017). The art and science of climate model tuning. *Bulletin of the American Meteorological Society*, *98*(3), 589–602. https://doi.org/10.1175/BAMS-D-15-00135.1

Jewtoukoff, V., Hertzog, A., Plougonven, R., Cámara, A. D. L., & Lott, F. (2015). Comparison of gravity waves in the southern hemisphere derived from balloon observations and the ECMWF Analyses. *Journal of the Atmospheric Sciences*, *72*(9), 3449–3468. https://doi.org/10.1175/JAS-D-14-0324.1

Kaifler, N., Kaifler, B., Dörnbrack, A., Rapp, M., Hormaechea, J. L., & de la Torre, A. (2020). Lidar observations of large-amplitude mountain waves in the stratosphere above Tierra del Fuego, Argentina. *Scientific Reports*, *10*(1), 14529. https://doi.org/10.1038/s41598-020-71443-7

Lott, F., & Miller, M. J. (1997). A new subgrid-scale orographic drag parametrization: Its formulation and testing. *Quarterly Journal of the Royal Meteorological Society*, *123*(537), 101–127. https://doi.org/10.1002/qj.49712353704

Lu, Y., Wu, T., Xu, X., Zhang, L., & Chu, M. (2020). Improved simulation of the Antarctic stratospheric final warming by modifying the orographic gravity wave parameterization in the Beijing climate center atmospheric general circulation model. *Atmosphere*, *11*(6), 576. https://doi.org/10.3390/atmos11060576

McLandress, C., Scinocca, J. F., Shepherd, T. G., Reader, M. C., & Manney, G. L. (2013). Dynamical control of the mesosphere by orographic and nonorographic gravity wave drag during the extended northern winters of 2006 and 2009. *Journal of the Atmospheric Sciences*, *70*(7), 2152–2169. https://doi.org/10.1175/JAS-D-12-0297.1

Orr, A., Bechtold, P., Scinocca, J., Ern, M., & Janiskova, M. (2010). Improved middle atmosphere climate and forecasts in the ECMWF model through a nonorographic gravity wave drag parameterization. *Journal of Climate*, *23*(22), 5905–5926. https://doi.org/10.1175/2010JCLI3490.1

Plougonven, R., la Cámara, A., Hertzog, A., & Lott, F. (2020). How does knowledge of atmospheric gravity waves guide their parameterizations? *Quarterly Journal of the Royal Meteorological Society*, *146*(728), 1529–1543. https://doi.org/10.1002/qj.3732

Plumb, R. A. (2002). Stratospheric transport. *Journal of the Meteorological Society of Japan*, *80*(4B), 793–809. https://doi.org/10.2151/jmsj.80.793

Polichtchouk, I., Shepherd, T. G., Hogan, R. J., & Bechtold, P. (2018). Sensitivity of the Brewer-Dobson circulation and polar vortex variability to parameterized nonorographic gravity wave drag in a high-resolution atmospheric model. *Journal of the Atmospheric Sciences*, *75*(5), 1525–1543. https://doi.org/10.1175/JAS-D-17-0304.1

Preusse, P., Dörnbrack, A., Eckermann, S. D., Riese, M., Schaeler, B., Bacmeister, J. T., et al. (2002). Space-based measurements of stratospheric mountain waves by CRISTA 1. Sensitivity, analysis method, and a case study. *Journal of Geophysical Research*, *107*(D23), 6–1. https://doi.org/10.1029/2001JD000699

Rapp, M., Kaifler, B., Dörnbrack, A., Gisinger, S., Mixa, T., Reichert, R., et al. (2020). SOUTHTRAC-GW: An airborne field campaign to explore gravity wave dynamics at the world's strongest hotspot. *Bulletin of the American Meteorological Society*, *1*, 1–60. https://doi.org/10.1175/BAMS-D-20-0034.1

Sato, K., Tateno, S., Watanabe, S., & Kawatani, Y. (2012). Gravity wave characteristics in the southern hemisphere revealed by a high-resolution middle-atmosphere general circulation model. *Journal of the Atmospheric Sciences*, *69*(4), 1378–1396. https://doi.org/10.1175/JAS-D-11-0101.1

Scinocca, J. F. (2002). The effect of back-reflection in the parameterization of non-orographic gravity-wave drag. *Journal of the Meteorological Society of Japan*, *80*(4B), 939–962. https://doi.org/10.2151/jmsj.80.939

Scinocca, J. F. (2003). An accurate spectral nonorographic gravity wave drag parameterization for general circulation models. *Journal of the Atmospheric Sciences*, *60*(4), 667–682. https://doi.org/10.1175/1520-0469(2003)060⟨0667:AASNGW⟩2.0.CO;2

Shibuya, R., Sato, K., Tomikawa, Y., Tsutsumi, M., & Sato, T. (2015). A study of multiple tropopause structures caused by inertia-gravity waves in the Antarctic. *Journal of the Atmospheric Sciences*, *72*(5), 2109–2130. https://doi.org/10.1175/JAS-D-14-0228.1

Shutts, G. J., & Vosper, S. B. (2011). Stratospheric gravity waves revealed in NWP model forecasts. *Quarterly Journal of the Royal Meteorological Society*, *137*(655), 303–317. https://doi.org/10.1002/qj.763

Watanabe, S., Sato, K., Kawatani, Y., & Takahashi, M. (2015). Vertical resolution dependence of gravity wave momentum flux simulated by an atmospheric general circulation model. *Geoscientific Model Development*, *8*(6), 1637–1644. https://doi.org/10.5194/gmd-8-1637-2015

Wu, D. L., & Eckermann, S. D. (2008). Global gravity wave variances from Aura MLS: Characteristics and interpretation. *Journal of the Atmospheric Sciences*, *65*(12), 3695–3718. https://doi.org/10.1175/2008JAS2489.1